



Role of Chromium Content on the Microstructure and Mechanical Properties of Lanthana Based Ferritic ODS Steels

Ashwani Kumar¹ · Bhagyaraj Jayabalan² · Chetan Singh³ · Jayant Jain³ · Subrata Mukherjee² · Krishanu Biswas¹ · Sudhanshu S. Singh¹

Received: 6 April 2022 / Accepted: 15 July 2022 / Published online: 23 August 2022
© The Author(s) under exclusive licence to The Korean Institute of Metals and Materials 2022

Abstract

In the current study, lanthana (La_2O_3) based oxide dispersion strengthened (ODS) ferritic steels ($\text{Fe}-x\text{Cr}-1\text{Ti}-1\text{W}-0.5\text{La}_2\text{O}_3$, $x = 14, 18, 22$, and 26 , in wt%) have been fabricated by mechanical alloying and spark plasma sintering. The role of chromium (Cr) content and maximum sintering temperature (1050 and 1100 °C) on the density, microstructure and mechanical properties of the ODS steels have been studied. TEM analysis of the alloy revealed the presence of nano-sized ($2-8$ nm) complex oxide particles, i.e., $\text{La}-\text{Ti}-\text{Cr}-\text{O}$. Mechanical properties were estimated in terms of micro-hardness, nano-hardness, Young's modulus and compressive strength. The highest micro-hardness (988 ± 11.3 HV) and compressive strength (2322 ± 49 MPa) were exhibited by the alloy having 26 wt% Cr, sintered at 1100 °C. The contribution of dispersion strengthening towards the strength was calculated to be the highest ($\sim 72\%$). Overall, increasing the Cr content improved both the room temperature compressive strength as well as the compressive fracture strain.

Keywords Mechanical alloying · Oxide particles · ODS steel · Lanthana · Spark plasma sintering

1 Introduction

Nanostructured oxide dispersion strengthened (ODS) ferritic steels are regarded as the most appropriate material for the next generation nuclear reactors [1, 2], in particular as cladding materials for core of the generation IV fast reactors. This is owing to their exceptional resistance to radiation (swelling), elevated temperature creep and oxidation/corrosion. Ferritic ODS steels typically contain a minimum of 12 wt% Cr, which provides stability to ferritic structure. Improved properties of the yttria (Y_2O_3) based ODS ferritic steels over their traditional ferritic compositions are

attributed to the presence of uniformly distributed nano-sized oxide particles i.e., dispersoids, which appear as obstacles to the movement of dislocations and are stable sinks for irradiation induced point defects (vacancy and interstitials) [3–5]. The addition of titanium (Ti) led to the formation of ~ 2 to 6 nm $\text{Y}-\text{Ti}-\text{O}$ nano-clusters, which further help in improving the high temperature strength and irradiation resistance [6–8].

ODS steels are normally produced by the powder metallurgy process which involves mechanical alloying (MA) and sintering, e.g., spark plasma sintering (SPS) [9–12], pressureless sintering [13], hot extrusion [14], high pressure sintering (HP) [15, 16] etc. SPS is a pressure assisted sintering method where total sintering time can be significantly shortened from hours to a few minutes. This results in smaller grain size and precipitates size, ensuing in improved mechanical properties [17]. In this regard, several studies have evaluated the effect of the various processing variables on the microstructure and mechanical properties of Y_2O_3 dispersed ODS steels consolidated by SPS. For instance, Dash et al. [18] performed ball milling followed by SPS to elucidate the evolution of nanocrystalline microstructure and creep behavior of 18-Cr ferritic ODS steels. Wu et al. [19] synthesized the mechanically alloyed

✉ Krishanu Biswas
kbiswas@iitk.ac.in

✉ Sudhanshu S. Singh
sudhanss@iitk.ac.in

¹ Department of Materials Science and Engineering,
Indian Institute of Technology Kanpur, Kanpur,
Uttar Pradesh 208016, India

² Research and Development, Tata Steel, Jamshedpur,
Jharkhand 831013, India

³ Department of Materials Science and Engineering, Indian
Institute of Technology Delhi, New Delhi 110016, India

Fe–16Cr–1Ti–3Mo–0.5Y₂O₃ ferritic steel using SPS and reported randomly orientated grains with bimodal grain size distribution and Y–Ti–Mo–Cr–O or Y–Mo–Cr–O oxide particles at and around grain boundaries. Li et al. [20] and Zhang et al. [21] observed the homogeneous dispersion of Y₂Ti₂O₇ nano-clusters in the 14Cr ODS steels consolidated by SPS.

It is evident that almost all studies on the ODS steels have focused on the use of Y₂O₃ and a very little attention has been paid to other potential rare earth oxides. Recently, Pasebani et al. [22] studied the possibility of using lanthana (La₂O₃) in place of Y₂O₃ in ODS steels. The rationale behind using La₂O₃ was its availability (bastnasite ore contains 32% of lanthana, whereas 0.1% of yttria) and being less costly than yttria [23]. In addition, insignificant solubility in iron at all temperatures and higher affinity of lanthanum towards oxygen were added advantages [23]. In the first investigation, Pasebani et al. [24] evaluated the role of milling duration on the microstructural evolution of Fe–14Cr–1Ti–0.3Mo–0.5La₂O₃ (14LMT) powders. The as-milled powders were observed to contain nano-clusters of TiO-, La- and O. In another study, 14LMT properties were measured and compared to Fe–14Cr–1Ti–0.3Mo–0.3Y₂O₃ (i.e., MA957) consolidated using the identical processing variables [25, 26]. The 14LMT alloy was observed to exhibit higher hardness than MA957 alloy. The ion irradiation did not bring a significant change in the number density and morphology of the nano-clusters, which indicated that La₂O₃ can serve as an alternative to Y₂O₃ [27].

In addition, it has been observed that tungsten (W) exhibits low activation and higher radioactive decay rate as compared to molybdenum (Mo) [28]. In addition, replacement of W in place of Mo has been shown to result in the similar or better mechanical properties of the ODS steels. With this background, the microstructure and mechanical properties of Fe–14Cr–1Ti–(0–2)W–0.5La₂O₃ ODS steels were investigated in our recent study [29]. It was found that the ODS steel, containing 1 wt% W, showed the highest hardness and compressive strength. The aim of present study is to elucidate the role of Cr content on the microstructure and mechanical properties of Fe–*x*Cr–1Ti–1W–0.5La₂O₃ (*x* = 14 to 26 wt%) ODS steels.

2 Materials and Experimental Details

2.1 Processing of Powders

The elemental powders of Cr (99.99% pure, 325 mesh), Ti (99.99% pure, 400 mesh) and La₂O₃ (99.99% pure, ~200 nm) were acquired from Alfa Aesar. W (99.99% pure, 400 mesh) and Fe (98.5% pure, 325 mesh) were acquired from Sigma Aldrich Inc. and Trixotech Ltd., respectively. The

Cryomilling of the as-received La₂O₃ powder was carried out for 5 h to decrease its average particle size. More details about the Cryomilling process and set up can be found in the previous studies [30, 31]. The pure elemental powders were first blended in proportion of Fe–*x*Cr–1Ti–1W–0.5La₂O₃ (*x* = 14–26 wt% in the step of 4). The blended powder compositions were subjected to ball milling, inside the two hardened stainless steel vials with hardened steel balls (weight of 0.5 g and 5 mm diameter), using a high energy planetary ball mill (Fritsch P6). The ball milling speed and ball to powder ratio (BPR) were maintained as 300 rpm and 10:1, respectively. The mechanical alloying was continued for 50 h. To inhibit the agglomeration and to lower the oxidation during milling, toluene was used as a milling media reagent. The initial blended powder compositions, subjected to ball milling are listed in Table 1.

2.2 Characterization of Ball Milled Powders

To identify and comprehend the phase evolution during mechanical alloying, the powders at various intervals of ball milling were investigated using PANalytical X'Pert X-ray diffraction (XRD). The Cu K α radiation, with wavelength of 1.5406 Å, was used during the experiment. Williamson–Hall formula [32] was utilized to estimate the accumulated lattice strain and mean crystallite size of the milled powders. To understand the morphology of the ball milled powders, FEI Nova 450 FESEM (field-emission scanning electron microscope) was utilized.

2.3 Spark Plasma Sintering

The powders were placed inside a high strength graphite die (cylindrical shape, inner diameter: 15 mm) and between the high strength graphite punches. A 250 μ m thin graphite sheet was also placed between die/punches and powders. The equipment set-up (Dr. Sinter 515 S apparatus; SPS Syntex Inc., Kanagawa, Japan) was used for the consolidation of powders.

Firstly, the SPS chamber was evacuated to 1.5×10^{-3} Torr vacuum level. It was followed by the purging of high pure (99.9% pure) argon gas. The process of evacuation and purging of high purity argon inside the SPS was carried out two times and subsequently argon was continuously purged

Table 1 Nominal compositions of initial powder blends (in wt%)

Alloy	Fe	Cr	Ti	W	La ₂ O ₃
A	83.5	14	1	1	0.5
B	79.5	18	1	1	0.5
C	75.5	22	1	1	0.5
D	71.5	26	1	1	0.5

during sintering. Applied pressure was gradually increased from 18 to 50 MPa within initial 4 min and then continued during the sintering cycle. The sintering was performed at the maximum temperature of 1050 and 1100 °C for 5 min using a heating rate of 100 °C/min. An optical pyrometer, focused on the central hole on the upper surface of the die, was used to monitor the temperature during the sintering cycle. After sintering, the consolidated samples were furnace cooled. The consolidated samples were typically in disk shape (height and diameter of 3 mm and 15 mm, respectively).

2.4 Microstructural Characterization of Sintered ODS Steels

The consolidated alloys were mechanically polished sequentially with SiC papers of different grit sizes (240–2000). This was followed by the cloth polishing with diamond paste (1 µm) and alumina suspension (0.3 µm). Lastly, the samples were mirror polished using colloidal silica solution (0.05 µm). A combination of XRD (using radiation of Cu-K α at a scan rate of 2°/min) and FESEM (FEI Nova 450) along with energy-dispersive spectroscopy (EDS) was used for the identification of phases in the consolidated alloys. The operating voltage used in SEM was 20 kV. Electron backscattered diffraction (EBSD) was performed in FESEM (JEOL 7800F with Oxford, Nordlys detector). During the EBSD scan, the probe current and step size were kept as ~14 nA and 0.2 µm, respectively. For post EBSD data analysis, HKL channel 5 software was utilized.

Transmission electron microscope (TEM, TALOS F200X) equipped with EDS was used for the nano-scale features studies of the sintered samples. The operating voltage was kept as 200 kV. Firstly, a 3 mm disk was machined out by spark erosion technique from the sample (100 µm thick). This was followed by dimpling (Model 656, Gatan, USA) to achieve 30 µm thick region at the disk's centre. Further, ion milling was carried out using a precision ion polishing system (PIPS, Model 691, Gatan, USA) to obtain electron transparent region. To minimize the localized heating and damaging of the sample, the ion milling parameters included the beam energy of 4 to 5 kV and incidence angle of 5°. The incidence angle was further lowered to 2° after initiation of perforation and kept at the same angle for 25 min to attain the electron transparent region needed for TEM observation.

2.5 Evaluation of Density and Mechanical Properties of the Sintered Alloys

Archimedes' method was used to determine the density of the sintered alloys. A minimum of five measurements were made for each specimen. The average densification of the specimens was reported as per their theoretical densities. A

universal Hardness Tester machine (FH-10, Tinius - olsen Ltd.) was used to measure the Vickers microhardness of the sample at load and dwell time of 1 kg and 10 s, respectively. For each specimen, 15 measurements were taken to ensure the reproducibility. The average value of micro-hardness was reported.

To calculate the Young's modulus and nano-hardness of the ODS steels, nanoindentation experiments were carried out using a ASMEC's Universal Nanomechanical Tester (Bautzner Landstraße 45, Germany) with a diamond Berkovich indenter. The indenter's calibration was carried out using standard fused quartz before actual indentations on the sintered samples. In an indentation cycle, both loading and unloading rates were kept as 10 mN/s. The peak load and dwell time at it were 500 mN and 10 s, respectively. Overall, 50 indentations were made on the sample.

For the compression tests, wire electrical discharge machining (EDM) was used to cut the cylindrical samples having diameter of 3 mm and thickness of 5 mm, respectively, maintaining the aspect ratio ~1.67 (ASTM standard E9). All the experiments were performed at room temperature at a strain rate of $1 \times 10^{-3} \text{ s}^{-1}$ in universal testing machine (Z030 TN Zwick/Roell). At least three samples were tested for each composition to confirm the repeatability of our results.

3 Results and Discussion

3.1 Microstructure Characterization of Mechanically Alloyed Powders

Figure 1a–d represent the XRD spectra of the four mechanically alloyed powder compositions (tabulated in Table 1) with milling time. The sharp crystalline diffraction peaks of Cr and Fe overlap with each other, whereas separate peaks of W are visible in the as-blended powders (0 h). The barely presence of peaks of L_2O_3 and Ti might be ascribed to their small volume fractions. Prominent detected diffraction peaks are at 44.73°, 64.67° and 82.43° after 50 h of ball milling. These angles correspond to (110), (200) and (211) planes of a body centred cubic (BCC) phase. Although a decrease in the intensities of the W peaks has been observed during milling, the XRD spectrum at 50 h still shows the peak of W. This suggests an incomplete dissolution of W in the ferritic matrix, which can be ascribed to the lower solubility of W in (Fe–Cr) matrix as per the equilibrium phase diagram and has also been stated in earlier studies [29, 33].

The observed peak broadening, with the progress of milling, could be attributed to the changes in the residual lattice strain and mean crystallite size. Figure 1e represents the evolution of induced lattice strain and crystallite size during ball milling. For all the alloys, the mean

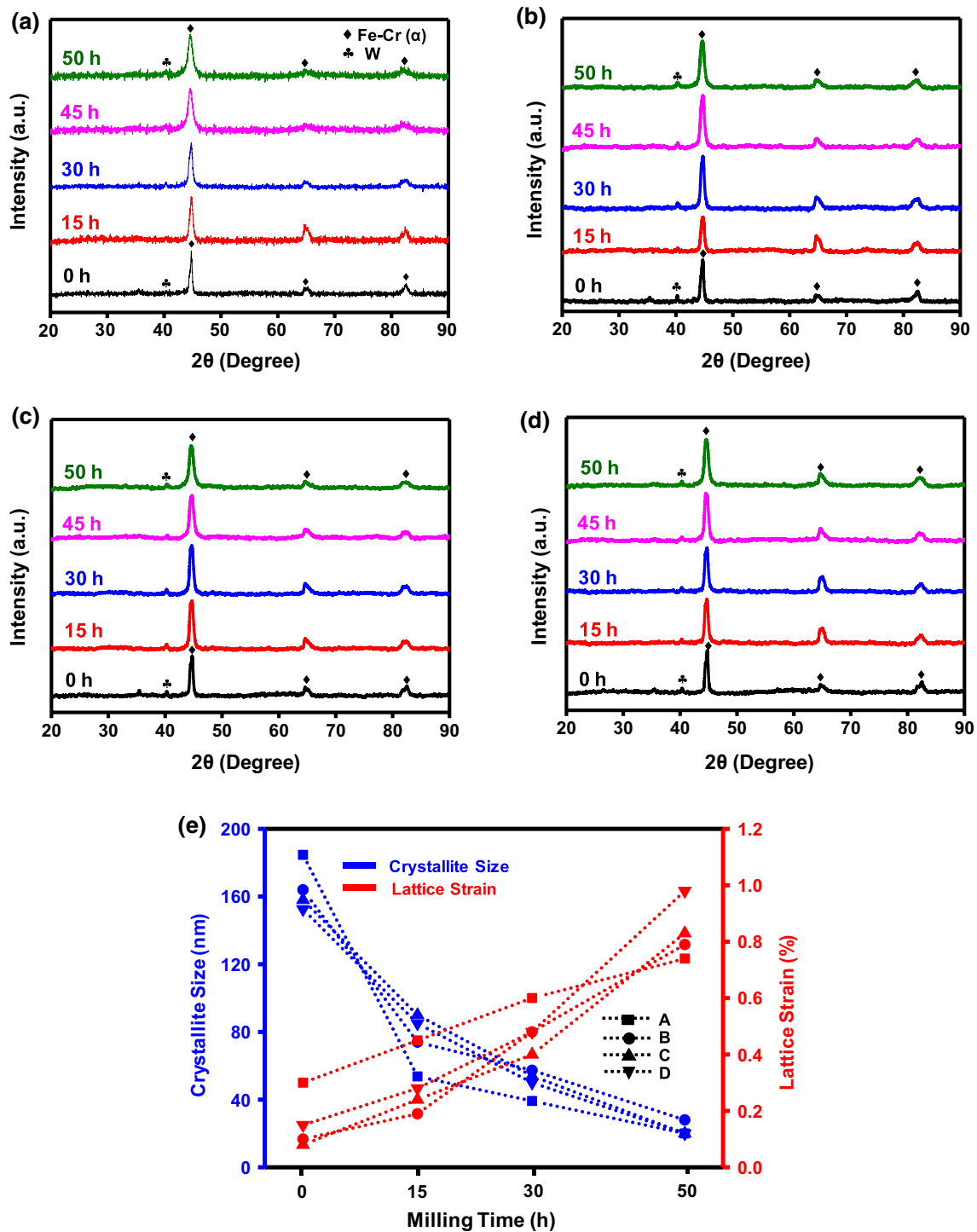


Fig. 1 XRD patterns with milling time for the ODS steel containing Cr content (wt%) of **a** 14 (alloy A), **b** 18 (alloy B), **c** 22 (alloy C), and **d** 26 (alloy D). **e** crystallite size and lattice strain of all the alloys after 50 h of mechanical alloying

crystallite size was observed to decrease with milling time. This indicates that the high energy ball milling effectively reduced the crystallite size of the powders. For instance, the crystallite size of alloy D decreased from 152 to 20 nm after 50 h of mechanical alloying.

On the contrary, milling resulted in an increase in the lattice strain. For instance, the lattice strain was found to increase to 0.98% in alloy D after 50 h of ball milling. This accumulated lattice strain may be ascribed to the severe plastic deformation and incorporation of crystal

imperfections due to mechanical alloying [22, 34]. It is apparent that the crystallite size reduction and the rise in the residual strain of all the four compositions are influenced by the Cr content. It can be noticed that the alloy D ball milled powder exhibits the smallest crystallite size (till 50 h) among all the alloys. Furthermore, the lattice strain of the alloy D is observed to be the highest among all the alloys. The SEM micrographs in Fig. 2a–d reveal the powders morphology of the alloy D after 0 h, 15 h, 30 h, and 50 h of mechanical alloying, respectively. It is evident that the particle size decreases with increase in milling time. The mean powder particle size was reduced from $22 \pm 9.4 \mu\text{m}$ to $3.5 \pm 0.87 \mu\text{m}$ after 50 h of mechanical alloying. This can be attributed to higher extent of solid solution strengthening with increase in the Cr content, which results in a higher degree of work hardening, and therefore greater reduction in the powder size. The irregular shaped powder particles can prominently be observed in the microstructure. Moreover, the observed powder morphology demonstrates that the mechanism during ball milling is similar to that of the ductile–brittle system [35]. EDS elemental maps of the marked region in Fig. 2 confirm the uniform distribution of all the major elements (i.e., Fe, Cr, W and Ti).

3.2 Microstructure Characterization of Sintered Alloys

Back-scattered electrons (BSE) images of alloy D, sintered at $1100 \text{ }^\circ\text{C}$, are shown in Fig. 3a. Based on the color contrast, the micrograph reveals two distinct phases, i.e., black colored phase distributed in the gray matrix. From the EDS area maps (Fig. 3a) and spectrum (Fig. 3b), it is evident that the matrix has a uniform distribution of all alloying elements. However, the dark phases are noticed to comprise of predominantly Cr and O. Figure 3c shows the XRD spectra of all the alloys after SPS at $1100 \text{ }^\circ\text{C}$, which highlight the predominant presence of BCC phase accompanied by small peaks of Cr_2O_3 . Furthermore, no W peak is observed in the XRD spectrum of alloy A sintered at $1100 \text{ }^\circ\text{C}$, indicating that the high temperature provided sufficient driving force for its dissolution in the ferrite matrix during sintering, as reported earlier [29]. In contrast, W peaks are visibly present in XRD spectrum of alloys B, C and D SPSed at $1100 \text{ }^\circ\text{C}$. It is possible that a higher content of Cr in these three alloys restricted the complete dissolution of W in the matrix. The results from EDS area maps and XRD spectra confirm that the gray matrix and dark phases are BCC and Cr_2O_3 , respectively. The formation of Cr_2O_3 in all the alloys might be ascribed to the high affinity of Cr towards O (or oxidation of Cr) at the sintering temperatures [36, 37].

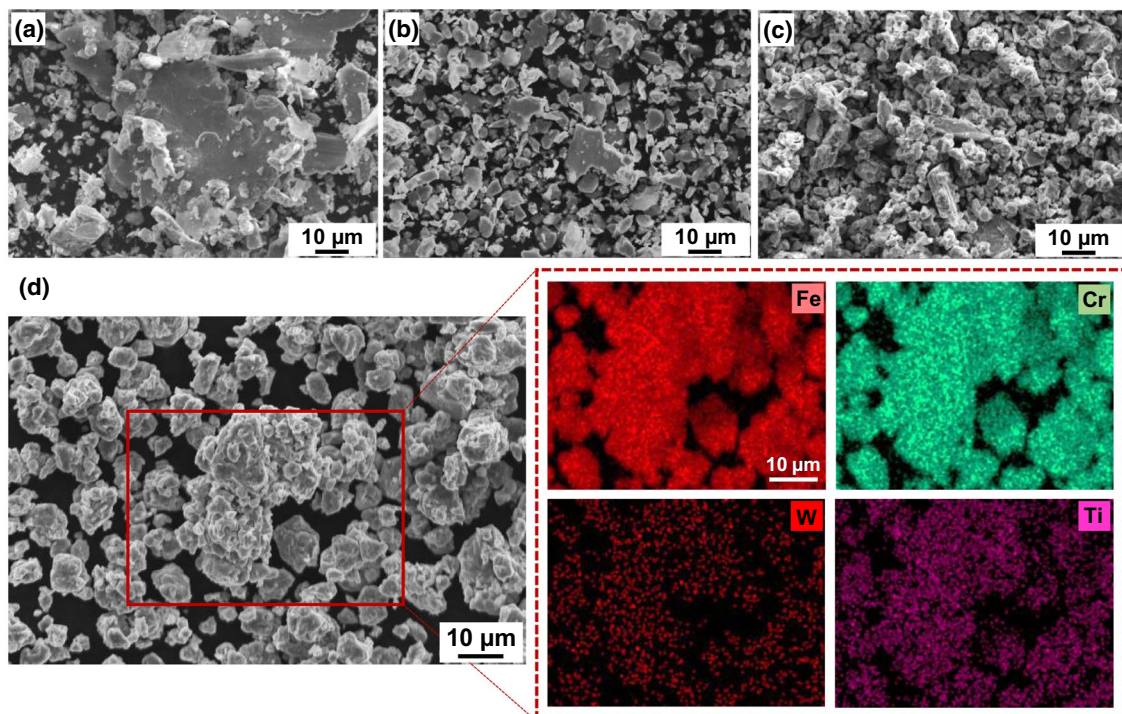


Fig. 2 SEM micrographs of the alloy D after **a** 0 h, **b** 15 h, **c** 30 h and **d** 50 h of mechanical alloying. EDS elemental maps correspond to 50 h powder

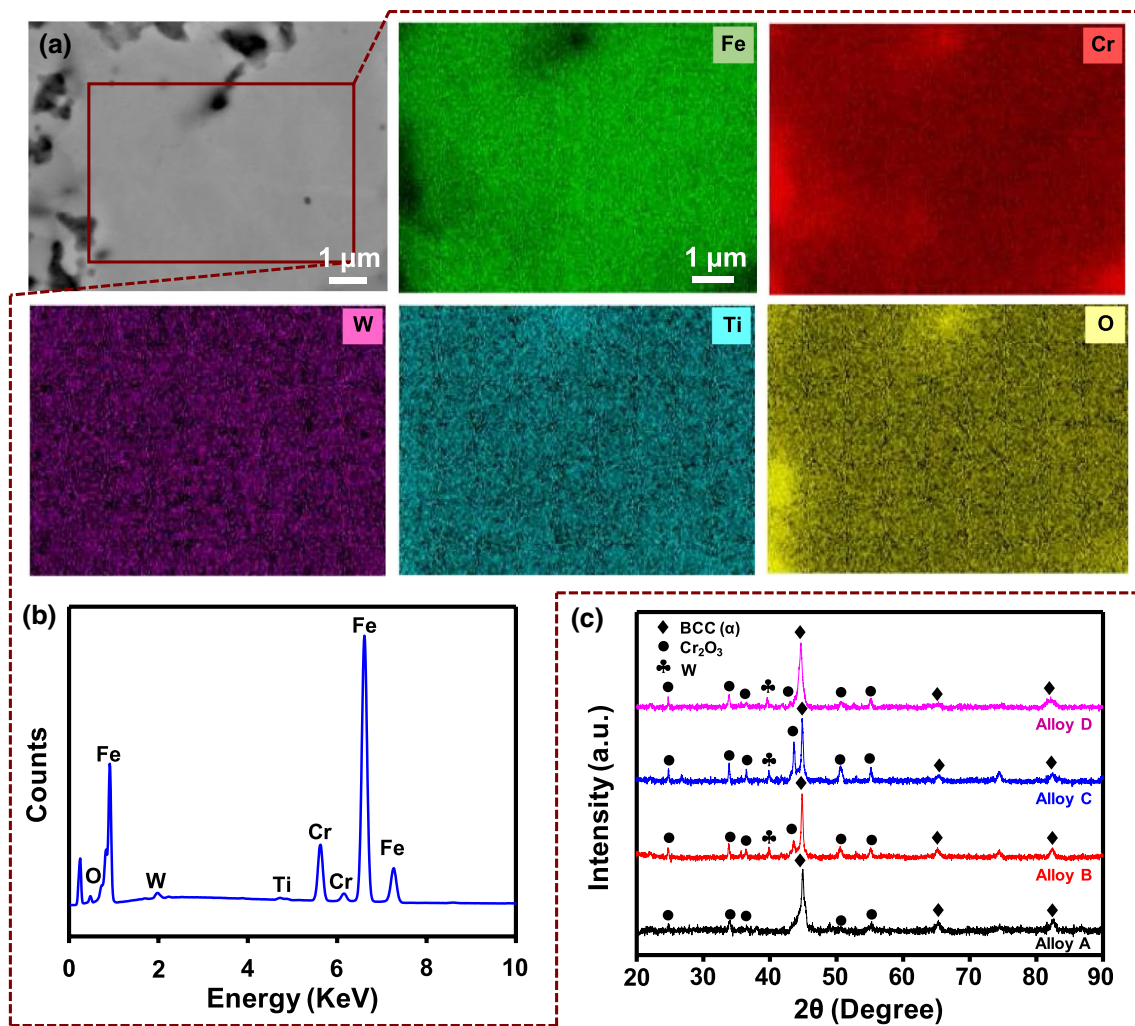


Fig. 3 a BSE micrograph along with elemental EDS area maps of alloy D after SPS and b corresponding EDS spectrum. (c) XRD patterns of alloys A, B, C and D sintered at 1100 °C

The IPF (inverse pole figure) maps of the alloy A and alloy D sintered at 1100 °C are depicted in Fig. 4a and d, respectively. It is evident that the grains are randomly oriented after sintering, which is in line with other studies [38]. The corresponding phase maps (Fig. 4b, e) reveal the presence of predominantly BCC phase in the microstructures, which confirms that both the alloys are ferritic, as also observed from the XRD analysis (Fig. 3). The grain size distributions for both the alloys are shown in Fig. 4c, f. It can be observed that most of the grains are below 2.5 μm in alloy D, whereas a large range of grain size is exhibited by alloy A. The mean grain size of the alloy A was calculated to be ~2.7 μm, whereas the mean grain size of the alloy D was ~1.2 μm. This indicates that increasing the Cr content resulted in a decrease in the grain size. Figure 5a and b show the typical bright field TEM images of alloy A and alloy D SPSed at 1100 °C, respectively. Fine grains with a wide grain size distribution (50 nm–1 μm) and high density of

dislocations in the darker contrast regions can be observed from the micrographs. Selected area electron diffraction patterns (SAEDPs) (Fig. 5a, b) show that the grains correspond to a BCC phase, i.e., ferrite matrix. Moreover, a heterogeneous dispersion of the nano-sized particles (or dispersoids) can also be observed in the alloys. It is pertinent to note that these nano-sized dispersoids are located at the triple points or along the grain boundaries, implying that these nano-sized particles can influence the recrystallization and further microstructure evolution during consolidation. The strained grains (due to mechanical alloying) are expected to recrystallize during sintering and further grain growth is expected to retard due to the existence of these nano-sized particles. Therefore, the observed grain size variation could be ascribed to the heterogeneous distribution of these nano-sized particles. This type of heterogeneous microstructure has also been outlined in earlier studies of ODS steels [26, 38]. Additionally, the existence of localized temperature

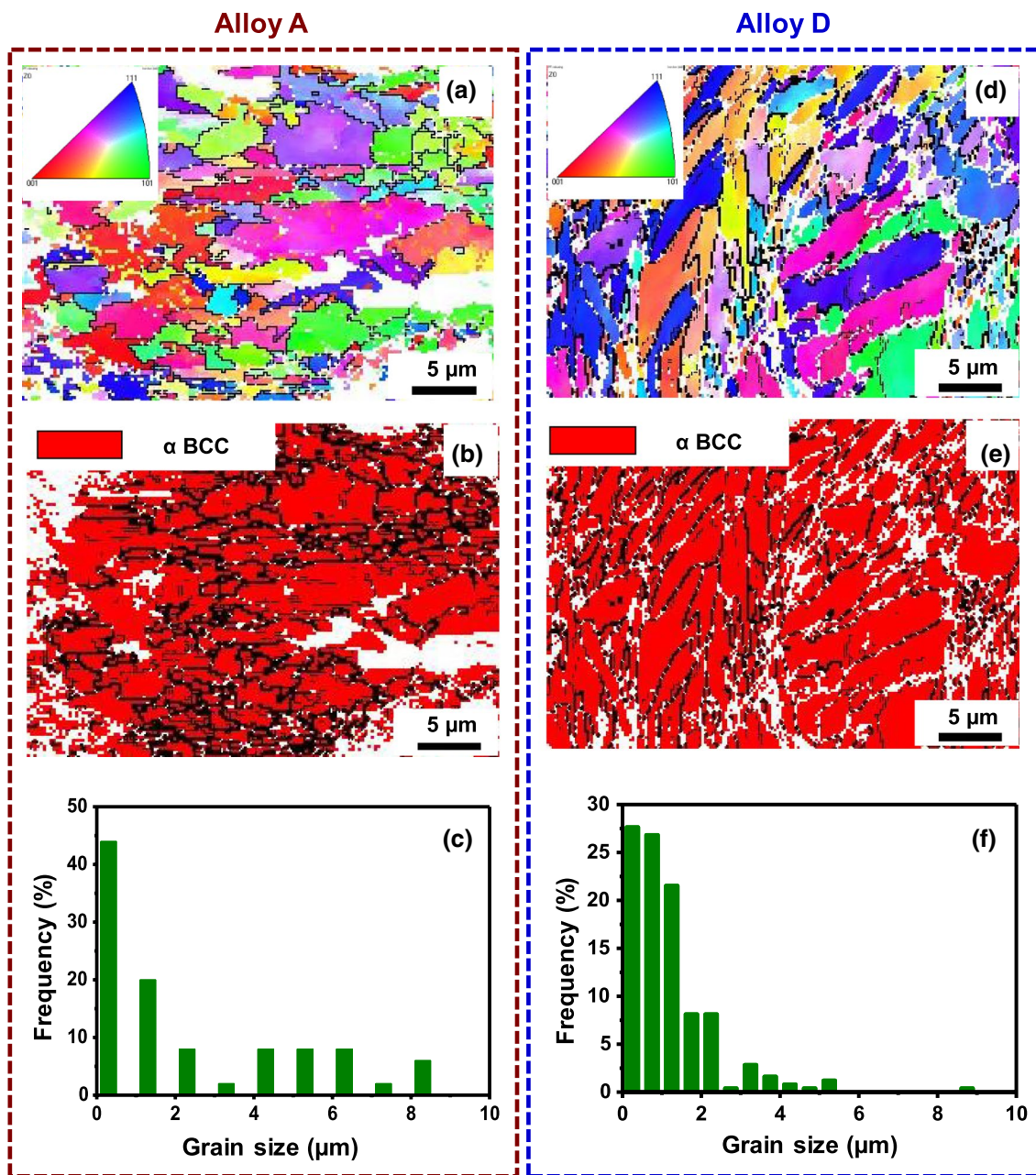


Fig. 4 a, d IPF map, b, e phase map, and c, f grain size distribution of the alloy A and alloy D sintered at 1100 °C, respectively

gradient during SPS has also been reported to yield both smaller and larger grains [26].

A high-resolution TEM image of the alloy D, SPSed at 1100 °C, is shown in Fig. 6a. It can be observed that spherical nano-sized particles are uniformly dispersed in this region. Figure 6b shows the size distribution of these particles. This indicates that the size of most of the particles falls between 2 and 6 nm (~84%) at the grain interior. The EDS spectrums obtained from the particle and the matrix are presented in Fig. 6c and d, respectively. The EDS results confirm that the particles are predominantly enriched in

La, O, Cr and Ti, whereas the matrix consists of Fe, Cr, W and Ti. It should be noted here that EDS may not give an accurate elemental quantification of the particles due to the contribution from the matrix. Therefore, no attempts were made to calculate the precise concentration of elements. In fact, peaks of Fe can be observed in the EDS spectrum of the particle (Fig. 6c). Nonetheless, the observed particles are likely to be complex La–Ti–Cr oxide (i.e., La–Ti–Cr–O), which has also been reported in the earlier studies [26]29. Apart from the grain refinement, these nano-sized oxide particles are also expected to contribute towards enhancing

Fig. 5 BF TEM micrographs of **a** alloy A and **b** alloy D sintered at 1100 °C

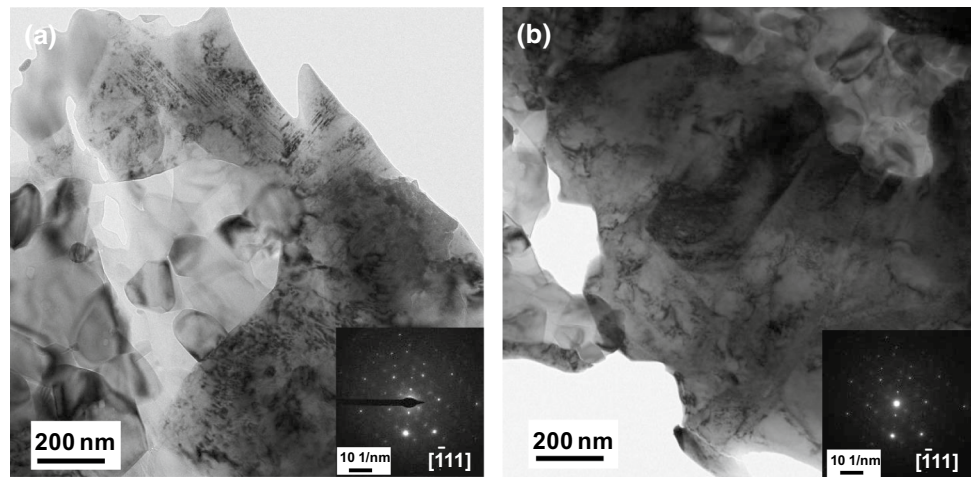
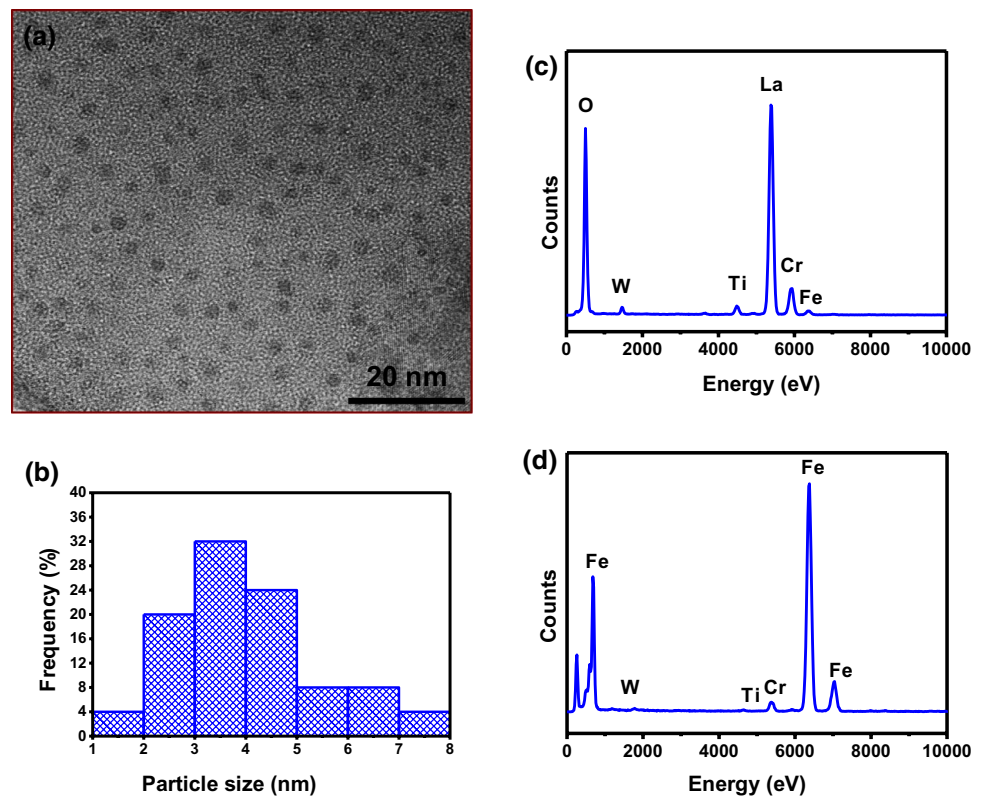


Fig. 6 **a** HRTEM micrograph showing dispersion of nano particles in the matrix of alloy D sintered at 1100 °C, **b** size distribution of these nano particles, **c, d** are TEM EDS spectrum of the nano particle and ferritic matrix, respectively



the strength of the alloys due to pinning of the movement of dislocations, i.e., dispersion strengthening.

3.3 Density Measurement and Mechanical Characterization of the Sintered Alloys

Figure 7a, b show the bulk density and micro-hardness of the sintered alloys with Cr content and maximum sintering temperature, respectively. A slight increase in density was noticed with Cr content. Furthermore, it increased with the maximum sintering temperature due to more significant

diffusional activity at a higher temperature. This is in line with the findings of the earlier studies [16]. It is observed that the micro-hardness of the sintered alloys increases with the Cr content as well as with the maximum sintering temperature. The alloy D, SPSed at 1100 °C, exhibits the highest microhardness of 988.5 ± 11.3 HV. The achieved hardness of the alloy D can be ascribed to a combined effect of at least three distinct strengthening mechanism, for instance solid solution strengthening, grain size strengthening and dispersion strengthening. All these mechanisms restrict the movement of the dislocation and therefore enhances the strength

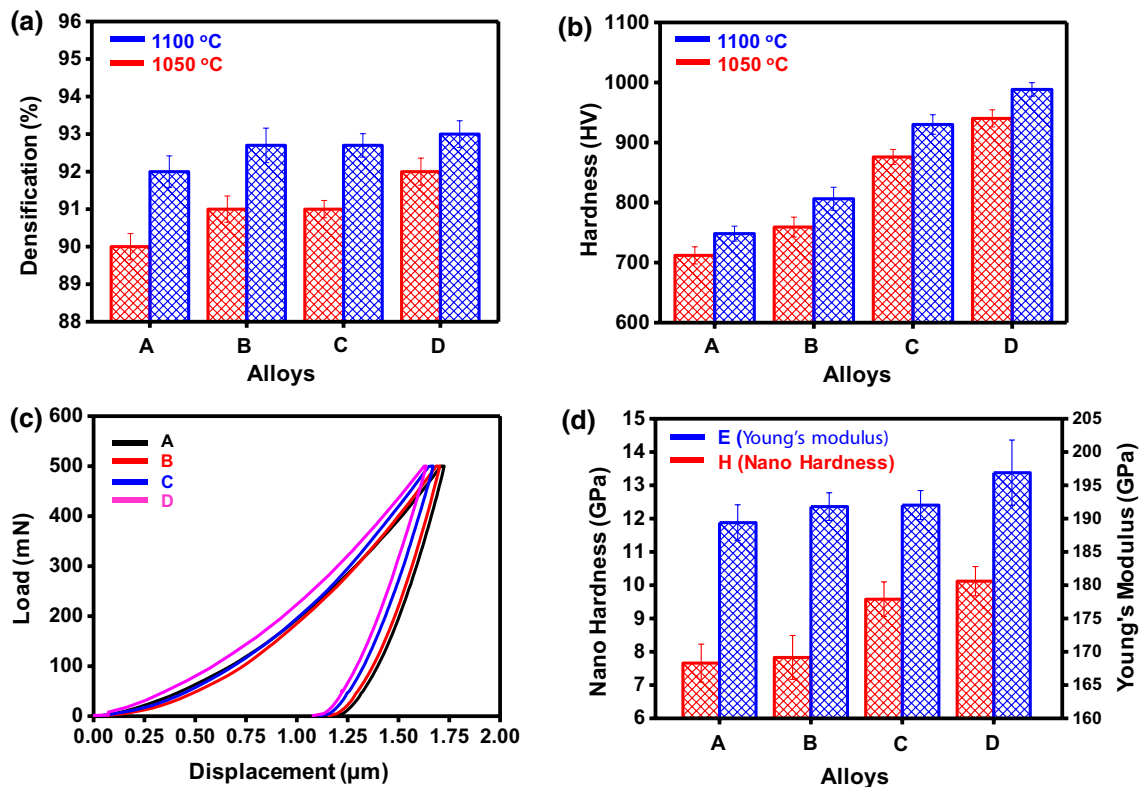


Fig. 7 **a** Densification and **b** Vickers micro-hardness of the alloys. **c** Load versus displacement curves and **d** variation of nano-hardness and Young's modulus of the alloys sintered at 1100 °C

of the alloy. Furthermore, the extent of contribution of all these strengthening mechanisms towards the strength of the alloy is anticipated to be different. The individual contribution of each of these mechanisms towards the strength of Alloy D will be discussed later.

Figure 7c represents the typical load vs. displacement plots of all the alloys SPSeD at 1100 °C. At the peak load, the lowest and highest attained indentation depth was exhibited by the alloy D (26 wt% Cr) and alloy A (14 wt% Cr), respectively. This also indicates that the alloy D and alloy A possess the highest and lowest nano-hardness, respectively. The nano-hardness values corroborate well with the Vickers micro-hardness values (Fig. 7b). The Young's modulus (E) of the sintered alloys was determined from the reduced modulus (E_r) and the properties of the indenter (E_i and ν_i) using the following equation:

$$\frac{1}{E_r} = \frac{1 - \nu^2}{E} + \frac{1 - \nu_i^2}{E_i} \quad (1)$$

For all the sintered alloys, the value of Poisson's ratio (ν) was assumed to be 0.3. Oliver and Pharr's method was used to determine the reduced modulus (E_r) from the slope of the unloading curve of load vs. displacement plot [39]. The nano-hardness was calculated from the ratio of the

maximum load and the indent projected area at the maximum load. Figure 7d represents the variation of the Young's modulus and nano-hardness with Cr content. It is evident that the trend followed by Young's modulus and nano-hardness is same as the trend of Vickers micro-hardness for all the sintered alloys. Alloy D is observed to exhibit the highest Young's modulus and nano-hardness of 196.9 ± 4.9 GPa and 10.12 ± 0.44 GPa, respectively. As mentioned before, the nano-hardness is contributed by a combined effect of at least grain boundary strengthening, solid solution strengthening, and dispersion strengthening.

Figure 8 presents the typical compressive stress vs. strain plots of all the alloys SPSeD at 1100 °C. It is observed that the compressive strength and fracture strain of the alloys are in the direct proportion to the Cr content. For instance, alloy D exhibits the highest compressive strength (2322 ± 49 MPa) with ductility of $\sim 6.5 \pm 0.1\%$, whereas alloy A exhibits the lowest compressive strength (1858 ± 53 MPa) with ductility of $\sim 4.1\%$. The increment in the compressive strength with respect to the Cr content was also observed by Karak et al. [34] in Fe- x Cr-2Al-0.5Ti-1.0Y₂O₃ (x varying from 13.5 to 25.5) ODS steels. Moreover, the strength of all the present alloys (La₂O₃-based ODS steels) is substantially higher than that of Y₂O₃-based ODS alloy MA957 (~ 1400 MPa), as reported by Klueh et al. [40]. Previously,

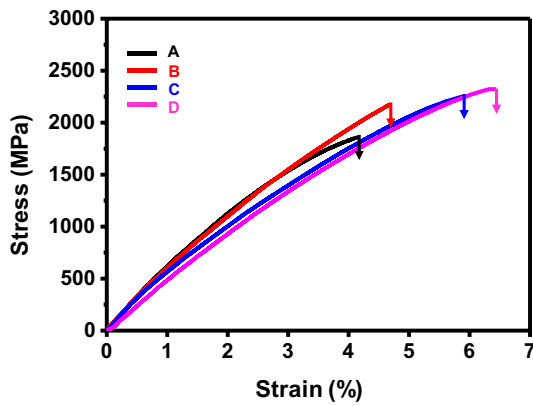


Fig. 8 Compressive stress–strain curves of all the studied alloys sintered at 1100 °C

Pasebani et al. [26] have explored the mechanical properties of Fe–14Cr–0.3Mo–1Ti–0.3Y₂O₃/La₂O₃, where La₂O₃ dispersed steels also exhibited a higher hardness (~505 HV) as compared to Y₂O₃-based steels (~460 HV).

The observed strength of the ODS steels could be ascribed to the combined effect of: (a) solid solution strengthening (σ_{ss}), predominantly due to Cr, (b) grain boundary strengthening due to grain refinement (σ_{GB}), (c) dispersion hardening from the nano-oxide particles (σ_d), (d) dislocation strengthening (σ_D), and (e) lattice friction (σ_o). Overall, all these mechanisms contribute towards restricting the mobility of dislocations through the lattice. Although the contribution of these strengthening mechanisms might be complex, for simplicity, the yield strength of the alloy can be assumed to be the linear summation of all the contributions as follows [25, 41]:

$$\sigma_y = \sigma_o + \sigma_{ss} + \sigma_D + \sigma_{GB} + \sigma_d \quad (2)$$

As the strength of alloy D is the highest, the contribution of all the aforementioned strengthening mechanisms to the strength of alloy D has been calculated. The composition (wt%) of alloy D is Fe–26Cr–1Ti–1W–0.5La₂O₃.

The contribution of solid solution strengthening can be expressed as:

$$\sigma_{ss} = \sum AC_i \quad (3)$$

where A is a coefficient and C_i is the element content in wt%. For the alloy D, since Ti is predominantly present in the nano-oxide particles and incomplete dissolution of W has also been observed, only Cr content has been considered for the solid solution strengthening. For Cr, A is equal to 8.5 MPa/wt% [25]. From Eq. (3), the contribution from the solid solution strengthening is calculated to be ~221 MPa.

The grain boundary strengthening contribution can be expressed by Hall–Petch relationship [42]:

$$\sigma_{GB} = kd^{-1/2} \quad (4)$$

where d and k are average grain diameter and Hall–Petch constant of the alloy, respectively. The value of k was taken to be 260 MPa· $\mu\text{m}^{0.5}$ for nano-structured ferritic steel [43]. From Eq. (4), the strength contribution by the grain boundaries is calculated to be ~237 MPa.

The contribution from dispersion strengthening can be expressed as [43]:

$$\sigma_d = k' \lambda_s^{-1/2} \quad (5)$$

$$\lambda_s = 1.22 \left\{ \left[\frac{\pi}{(4f_v)} \right] 0.5 - 1 \right\} d \quad (6)$$

where k' is a constant (395 MPa $\mu\text{m}^{0.5}$) and λ_s is the inter-particle spacing [43]. Volume fraction (f_v) is the volume fraction and d is the average size of the nano-oxide particles. f_v can be calculated from La₂O₃ content as [42]:

$$f_v = 1.5618 \times 10^{-2} \times (\text{wt\% lanthana}) \quad (7)$$

From Eqs. (5) and (6), σ_d is roughly calculated to be ~1682 MPa by taking f_v as 0.0078 (from Eq. 7). ‘ d ’ was taken as 5 nm, which is the approximate average size of the oxide particles (Fig. 6b). For overall strength of alloy D, the contribution from solid solution strengthening, grain size strengthening and dispersion strengthening are ~221 MPa, ~237 MPa, and ~1682 MPa, respectively. Rest of the strength contribution (i.e., 182 MPa) is originating from the dislocation strengthening (σ_D) and friction stress (σ_o). Overall, the contribution from the dispersion strengthening is the highest (~72%) followed by grain boundary strengthening (~10%) and solid solution strengthening (~9.5%).

4 Conclusions

In this study, the influence of Cr content on the microstructure and mechanical properties of La₂O₃ dispersed ODS ferritic steels have been examined. The key conclusions are summarized below:

- (1) For all the alloys, mechanical alloying led to the formation of BCC (α -Fe) matrix along with some undissolved W.
- (2) The Young’s modulus and hardness of the alloys increased with both the maximum sintering temperature and Cr content. The alloy D SPSed at 1100 °C possessed the highest hardness and Young’s modulus of 988.5 ± 11.3 HV and 196.9 ± 4.9 GPa, respectively.
- (3) TEM analysis showed the heterogeneous dispersion of 2 to 6 nm La–Ti–Cr–O complex oxides.

- (4) The alloy D exhibited the highest compressive strength and ductility of 2322 ± 49 MPa and $6.5 \pm 0.1\%$, respectively, which was attributed to the solid solution strengthening, grain refinement and dispersion hardening.
- (5) For the alloy D, overall estimated strengthening contribution from the dispersion strengthening is the highest ($\sim 72\%$) followed by grain boundary strengthening ($\sim 10\%$) and solid solution strengthening ($\sim 9.5\%$).

Acknowledgements SSS and KB thank Science and Engineering Research Board (India) for the research funding (Grant No: ECR/2016/001411). Authors acknowledge the characterization facilities at the Materials Science and Department of Materials Science and Engineering and Advanced Center for Materials Science (ACMS) at IIT Kanpur. Authors also acknowledge the TEM facility of Advanced Materials & Characterization Research Group of R&D, Tata Steel.

Author Contributions AK: conceptualization, investigation, methodology, writing—original draft. JB: investigation, methodology. CS: investigation, methodology. JJ: conceptualization, resources, writing—review & editing. SM: conceptualization, resources, writing—review & editing. KB: conceptualization, resources, supervision, writing—review & editing, funding acquisition. SSS: conceptualization, resources, supervision, writing—review & editing, funding acquisition.

Data Availability The raw/processed data required to reproduce these findings cannot be shared at this time as the data also forms part of an ongoing study.

Declarations

Conflict of interests The authors declare that they have no known competing financial interests or personal relationships that could have appeared to influence the work reported in this paper.

References

1. T. Jayakumar, M.D. Mathew, K. Laha, R. Sandhya, Nucl. Eng. Des. **265**, 1175 (2013). <https://doi.org/10.1016/j.nucengdes.2013.05.001>
2. T.K. Kim, S. Noh, S.H. Kang, H.J. Jin, G.E. Kim, World J Eng. Technol. **3**, 125 (2015). <https://doi.org/10.4236/wjet.2015.33c019>
3. S.K. Karak, T. Chudoba, Z. Witzczak, W. Lojkowski, I. Manna, Mater. Sci. Eng. A **528**, 7475 (2011). <https://doi.org/10.1016/j.msea.2011.06.039>
4. G. Sundararajan, R. Vijay, A.V. Reddy, Curr. Sci. **105**, 1100 (2013)
5. D.K. Mukhopadhyay, F.H. Froes, D.S. Gelles, J. Nucl. Mater. **258–263**, 1209 (1998). [https://doi.org/10.1016/S0022-3115\(98\)00188-3](https://doi.org/10.1016/S0022-3115(98)00188-3)
6. M. Ratti, D. Leuvrey, M.H. Mathon, Y. de Carlan, J. Nucl. Mater. **386–388**, 540 (2009). <https://doi.org/10.1016/j.jnucmat.2008.12.171>
7. M.J. Alinger, G.R. Odette, D.T. Hoelzer, J. Nucl. Mater. **329–333**, 382 (2004). <https://doi.org/10.1016/j.jnucmat.2004.04.042>
8. S.V. Rogozhkin, A.A. Bogachev, D.I. Kirillov, A.A. Nikitin, N.N. Orlov, A.A. Aleev, A.G. Zaluzhnyi, M.A. Kozodaev, Phys. Metals Metallogr. **115**, 1259 (2014). <https://doi.org/10.1134/S0031918X14120060>
9. W. Li, H. Xu, X. Sha, J. Meng, W. Wang, C. Kang, X. Zhang, Z. Wang, Fusion Eng. Des. **137**, 71 (2018). <https://doi.org/10.1016/j.fusengdes.2018.08.020>
10. Q. Zhao, Z. Qiao, Y. Liu, L. Yu, Y. Huang, Q. Guo, H. Li, Metals **9**, 200 (2019). <https://doi.org/10.3390/met9020200>
11. M.S. Staltsov, I.I. Chernov, I.A. Bogachev, B.A. Kalin, E.A. Olevsky, L.J. Lebedeva, A.A. Nikitina, Nucl. Mater. Energy **9**, 360 (2016). <https://doi.org/10.1016/j.nme.2016.08.020>
12. A. Kumar, B. Jayabalan, C. Singh, J. Jain, S. Mukherjee, K. Biswas, S.S. Singh, Mater. Sci. Eng. A **837**, 142746 (2022). <https://doi.org/10.1016/j.msea.2022.142746>
13. Q.X. Sun, T. Zhang, X.P. Wang, Q.F. Fang, T. Hao, C.S. Liu, J. Nucl. Mater. **424**, 279 (2012). <https://doi.org/10.1016/j.jnucmat.2011.12.020>
14. I. Hilger, X. Boulnat, J. Hoffmann, C. Testani, F. Bergner, Y. De Carlan, F. Ferraro, A. Ulbricht, J. Nucl. Mater. **472**, 206 (2016). <https://doi.org/10.1016/j.jnucmat.2015.09.036>
15. Z. Oksiuta, A. Ozieblo, K. Perkowski, M. Osuchowski, M. Lewandowska, Fusion Eng. Des. **89**, 137 (2014). <https://doi.org/10.1016/j.fusengdes.2014.01.052>
16. S.K. Karak, J. Dutta Majumdar, Z. Witzczak, W. Lojkowski, Ł Ciupiński, K.J. Kurzydłowski, I. Manna, Metall. Mater. Trans. A **44**, 2884 (2013). <https://doi.org/10.1007/s11661-013-1627-9>
17. O. Guillon, J. Gonzalez-Julian, B. Dargatz, T. Kessel, G. Schierning, J. Räthel, M. Herrmann, Adv. Eng. Mater. **16**, 830 (2014). <https://doi.org/10.1002/adem.201300409>
18. M.K. Dash, R. Mythili, R. Ravi, T. Sakthivel, A. Dasgupta, S. Saroja, S.R. Bakshi, Mater. Sci. Eng. A **736**, 137 (2018). <https://doi.org/10.1016/j.msea.2018.08.093>
19. Y.Q. Wu, K.N. Allahar, J. Burns, B. Jaques, I. Charit, D.P. Butt, J.I. Cole, Cry. Res. Tech. **49**, 645 (2014). <https://doi.org/10.1002/crat.201300173>
20. Z. Li, Z. Lu, R. Xie, C. Lu, C. Liu, Mater. Sci. Eng. A **660**, 52 (2016). <https://doi.org/10.1016/j.msea.2016.02.073>
21. H. Zhang, Y. Huang, H. Ning, C.A. Williams, A.J. London, K. Dawson, Z. Hong, M.J. Gorley, C.R.M. Grovenor, G.J. Tatlock, S.G. Roberts, M.J. Reece, H. Yan, P.S. Grant, J. Nucl. Mater. **464**, 61 (2015). <https://doi.org/10.1016/j.jnucmat.2015.04.029>
22. S. Pasebani, I. Charit, D.P. Butt, J.I. Cole, J. Nucl. Mater. **434**, 282 (2013). <https://doi.org/10.1016/j.jnucmat.2012.11.020>
23. G. Tyler, Plant Soil **267**, 191 (2004). <https://doi.org/10.1007/s11104-005-4888-2>
24. S. Pasebani, I. Charit, Y.Q. Wu, D.P. Butt, J.I. Cole, Acta Mater. **61**, 5605 (2013). <https://doi.org/10.1016/j.actamat.2013.06.002>
25. S. Pasebani, I. Charit, Y. Wu, J. Burns, K.N. Allahar, D.P. Butt, J.I. Cole, S.F. Alsagabi, J. Nucl. Mater. **470**, 297 (2016). <https://doi.org/10.1016/j.jnucmat.2015.12.035>
26. S. Pasebani, I. Charit, D.P. Butt, J.I. Cole, Y. Wu, J. Burns, Adv. Eng. Mater. **18**, 324 (2016). <https://doi.org/10.1002/adem.20150294>
27. S. Pasebani, I. Charit, A. Guria, Y. Wu, J. Burns, D.P. Butt, J.I. Cole, L. Shao, J. Nucl. Mater. **495**, 78 (2017). <https://doi.org/10.1016/j.jnucmat.2017.08.010>
28. F. Abe, T. Noda, H. Araki, M. Okada, Optimization of reduced activation ferritic steels, in *Reduced Activation Materials for Fusion Reactors*, 2009. <https://doi.org/10.1520/stp24954s>
29. A. Kumar, J. Bhagyaraj, A. Prasad, J. Jain, S. Mukherjee, K. Biswas, S.S. Singh, Mater. Sci. Eng. A **828**, 142077 (2021). <https://doi.org/10.1016/j.msea.2021.142077>
30. N. Kumar, K. Biswas, Rev. Sci. Instrum. **86**, 083903 (2015). <https://doi.org/10.1063/1.4929325>
31. N.K. Katiyar, K. Biswas, C.S. Tiwary, Int. Mater. Rev. **66**, 493 (2021). <https://doi.org/10.1080/09506608.2020.1825175>

32. V. Mote, Y. Purushotham, B. Dole, J. Theor. Appl. Phys. **6**, 6 (2012). <https://doi.org/10.1186/2251-7235-6-6>
33. B. Dousti, R. Mojaver, H.R. Shahverdi, R.S. Mamoory, J. Alloy. Compd. **577**, 409 (2013). <https://doi.org/10.1016/j.jallcom.2013.05.201>
34. S.K. Karak, J.D. Majumdar, W. Lojkowski, A. Michalski, L. Ciupinski, K.J. Kurzydowski, I. Manna, Philos. Mag. **92**, 516 (2012). <https://doi.org/10.1080/14786435.2011.619508>
35. C. Suryanarayana, Prog. Mater. Sci. **46**, 1 (2001). [https://doi.org/10.1016/S0079-6425\(99\)00010-9](https://doi.org/10.1016/S0079-6425(99)00010-9)
36. B. Patel, F. Inam, M.J. Reece, M. Edirisinghe, W. Bonfield, J. Huang, A. Angadji, Adv. Eng. Mater. **13**, 411 (2011). <https://doi.org/10.1002/adem.201000367>
37. S. Pasebani, I. Charit, J. Alloy. Compd. **599**, 206 (2014). <https://doi.org/10.1016/j.jallcom.2014.01.243>
38. A. Meza, E. Macía, A. García-Junceda, L.A. Díaz, P. Chekhonin, E. Altstadt, M. Serrano, M.E. Rabanal, M. Campos, Metals **10**, 1344 (2020). <https://doi.org/10.3390/met10101344>
39. W.C. Oliver, G.M. Pharr, J. Mater. Res. **7**, 1564 (1992). <https://doi.org/10.1557/jmr.1992.1564>
40. R.L. Klueh, P.J. Maziasz, I.S. Kim, L. Heatherly, D.T. Hoelzer, N. Hashimoto, E.A. Kenik, K. Miyahara, J. Nucl. Mater. **307–311**, 773 (2002). [https://doi.org/10.1016/S0022-3115\(02\)01046-2](https://doi.org/10.1016/S0022-3115(02)01046-2)
41. J. Shen, Y. Li, F. Li, H. Yang, Z. Zhao, S. Kano, Y. Matsukawa, Y. Satoh, H. Abe, Mater. Sci. Eng. A **673**, 624 (2016). <https://doi.org/10.1016/j.msea.2016.07.030>
42. X. Zhou, Y. Liu, L. Yu, Z. Ma, Q. Guo, Y. Huang, H. Li, Mater. Design **132**, 158 (2017). <https://doi.org/10.1016/j.matdes.2017.06.063>
43. B. Srinivasarao, K. Oh-ishi, T. Ohkubo, K. Hono, Acta Mater. **57**, 3277 (2009). <https://doi.org/10.1016/j.actamat.2009.03.034>

Publisher's Note Springer Nature remains neutral with regard to jurisdictional claims in published maps and institutional affiliations.

Springer Nature or its licensor holds exclusive rights to this article under a publishing agreement with the author(s) or other rightsholder(s); author self-archiving of the accepted manuscript version of this article is solely governed by the terms of such publishing agreement and applicable law.